RSC Advances

PAPER

View Article Online
View Journal | View Issue

Cite this: *RSC Adv.*, 2021, **11**, 17622

Thermal, ferroelastic, and structural properties near phase transitions of organic–inorganic perovskite type $[NH_3(CH_2)_3NH_3]CdBr_4$ crystals

Ae Ran Lim *[ab]

Hybrid perovskites have potential applications in several electrochemical devices such as supercapacitors, batteries, and fuel cells. Therefore, we studied the thermal behavior and structural dynamics of organic–inorganic hybrid perovskite $[(NH_3)(CH_2)_3(NH_3)]CdBr_4$ crystals near phase transition temperatures, T_{C2} (=328 K) and T_{C1} (=363 K), which are correlated to the structural dynamics of cations and anions. The structural geometry and molecular dynamics with emphasis on the role of the $[(NH_3)(CH_2)_3(NH_3)]$ cation and $CdBr_6$ anion were discussed in terms of MAS ^1H NMR, MAS ^{13}C NMR, ^{14}N NMR, and ^{113}Cd NMR as a function of the temperature. The environments surrounding ^1H, ^{13}C, ^{14}N, and ^{113}Cd are investigated near T_{C1} and T_{C2} using these results. Spin–lattice relaxation times $T_{1\rho}$ were discussed in terms of the change in temperature. The discontinuous changes of ^1H $T_{1\rho}$ and ^{13}C $T_{1\rho}$ near T_{C1} are consistent with the change of the lattice constant. Shorter $T_{1\rho}$ values at high temperature indicate that ^1H and ^{13}C in the organic chains are more flexible at these temperatures. Based on these results, the physicochemical properties of the cation and anion during the III–II–I phase transitions were discussed. This study was conducted to improve the relatively weak thermal stability compared to the high efficiency for a variety of applications.

Received 15th March 2021
Accepted 8th May 2021

DOI: 10.1039/d1ra02045e

rsc.li/rsc-advances

I. Introduction

Organic–inorganic compounds based on two-dimensional (2D) hybrid perovskites, particularly $[(C_nH_{2n+1}NH_3)]_2BX_4$ (n = 1, 2, 3,…; B = Mn, Co, Cu, Zn, Cd; X = Cl, Br) and $[NH_3(CH_2)_nNH_3]BX_4$ (n = 2, 3,…), have attracted considerable attention in recent years. The monoammonium $[(C_nH_{2n+1}NH_3)]_2BX_4$ (ref. 1–7) and diammonium $[NH_3(CH_2)_nNH_3]BX_4$ series have been extensively studied owing to their relative stability and potential applications.[8–13] The properties and structural phase transitions of organic–inorganic hybrid perovskites are related to their structures and the interaction of cationic units with complex anionic sublattices.[14] The phase transitions for diammonium $[NH_3(CH_2)_nNH_3]BX_4$ compounds have their origin in the dynamics of the cations, in particular from the dynamics of the NH_3 groups forming hydrogen bonds with the halogen atoms of the anion layers and hindered rotational motions of the entire alkyl group around the long molecular axis.[10] For B = Mn, Cu, or Cd, the structure consists of the corner shared octahedral $(BX_6)^{2-}$ alternated with organic layers. In contrast, for B = Co or Zn, isolated tetrahedral structures are formed in the inorganic layer $(BX_4)^{2-}$ sandwiched between layers of organic cations.[15–23] These compounds have attracted attention owing to the multiplicity of their crystal structures, which is correlated to the structural dynamics of cations and anions. Ferroelasticity is commonly observed in materials with a perovskite crystal structure. Recently, the ferroelastic twin domain observed in organic–inorganic hybrid perovskite likewise garnered significant attention.[24–27] 2D hybrid perovskites are promising for a variety of applications, including photovoltaics, photocatalysis, batteries, and energy storage.[28,29]

The $[NH_3(CH_2)_3NH_3]CdBr_4$ (1,3-propanediammonium tetrabromocadmate) crystal (n = 3; B = Cd; X = Br), a member of the diammonium $[NH_3(CH_2)_nNH_3]BX_4$ series, belongs to the orthorhombic structure at room temperature. This crystal with Cd is a very special case; it exhibits an unusual phase sequence, *i.e.*, its stable phase at the highest temperature is the one with the lowest symmetry.[30] This crystal undergoes two phase transitions, at temperatures of 326 K (=T_{C2}) and 368 K (=T_{C1}).[10,30] The room temperature phase III was determined in the space group *Pnma* (point group *mmm*) of the orthorhombic structure. Its lattice constants have been reported as a = 7.721 Å, b = 19.054 Å, c = 7.898 Å, and Z = 4.[30] In this phase, Cd atoms are surrounded by six bromine atoms forming a nearly regular octahedron $CdBr_6$. Of these six bromine atoms, four Br atoms are bridging atoms shared with the neighboring octahedral, and two Br atoms are terminal atoms resulting in bidimensional anion planes. These formations are connected by hydrogen bonds N–H···Br and the cation. The phase II above

[a]*Department of Carbon Convergence Engineering, Department of Science Education, Jeonju University, Jeonju 55069, Korea. E-mail: aeranlim@hanmail.net; arlim@jj.ac.kr*

[b]*Analytical Laboratory of Advanced Ferroelectric Crystals, Jeonju University, Jeonju 55069, Korea*

T_{C2} has the space group *Ima*2 (point group *mmm*) and the same orthorhombic structure. In the highest phase I, this crystal is in the monoclinic structure with the space group $P2_1/m$ (point group $2/m$). The lattice constants a and b increase continuously with rising temperature, but the value of c decreases slightly at T_{C2} and shortens rapidly at T_{C1}. The monoclinic angle β abruptly increases with increasing temperature, reaching approximately 95.5° in this phase, whereas in phases II and III, its value was constant at $\beta = 90°$.[30]

For $[NH_3(CH_2)_3NH_3]CdBr_4$ crystals, a temperature dependence experiment addressing the $^{79,81}Br$ nuclear quadrupole resonance (NQR) near the phase transition temperatures was studied by Ishihara *et al.*[31,32] The X-ray structure analysis at room temperature was likewise reported.[32] Further, the spectroscopic properties of this crystal with its phase sequence were investigated *via* various experimental methods: differential scanning calorimetry (DSC), infrared (IR), far infrared (FIR), and Raman spectroscopy measurements.[10] Recently, optical and dilatometric studies presented the multidomain states obtained by optical polarizing microscopic observation.[14] Although $[NH_3(CH_2)_3NH_3]CdBr_4$ has numerous applications, the physicochemical properties and molecular dynamics of its crystals have not been studied to date.

In this study, the structure and phase transition temperatures of $[NH_3(CH_2)_3NH_3]CdBr_4$ crystals are investigated *via* X-ray diffraction and DSC. Thermogravimetric analysis (TGA) and differential thermal analysis (DTA) experiments were performed to obtain a better understanding of the thermal properties. The chemical shifts and molecular dynamics were probed by ^1H magic-angle spinning nuclear magnetic resonance (MAS NMR) and ^{13}C MAS NMR as a function of temperature to elucidate the role of the $[NH_3(CH_2)_3NH_3]$ cation. Furthermore, the chemical shifts for ^{14}N and ^{113}Cd of the $CdBr_6$ anion were recorded by static NMR spectra as a function of the temperature. The spin–lattice relaxation times ($T_{1\rho}$) in the rotating frame were discussed in terms of the change of temperature. Based on these results, the structural dynamics of the $[NH_3(CH_2)_3NH_3]$ cation and $CdBr_4$ anion during the III–II–I phase transitions were discussed. The ferroelastic twin domain walls in all phases were observed as well. Finally, we compare the physicochemical properties of $[NH_3(CH_2)_3NH_3]CdBr_4$ with those of $[NH_3(CH_2)_3NH_3]CdCl_4$ previously reported. Moreover, the physicochemical properties revealed important information regarding the basic mechanisms that enable their widespread applicability.

II. Experimental method

An aqueous solution containing $NH_2(CH_2)_3NH_2 \cdot 2HBr$ and $CdBr_2$ was slowly evaporated at a constant temperature of 300 K to yield single crystals of $[NH_3(CH_2)_3NH_3]CdBr_4$. The $[NH_3(CH_2)_3NH_3]CdBr_4$ single crystal grown here has a colorless and transparent square shape.

The structure of the $[NH_3(CH_2)_3NH_3]CdBr_4$ crystal at 298 K was analyzed using an X-ray diffraction system equipped with a Cu-Kα radiation source. The lattice parameters were determined by single crystal X-ray diffraction at the Western Seoul Center of Korea Basic Science Institute (KBSI). The crystals were mounted on a Bruker D8 Venture equipped with an I μS microfocus sealed tube Mo-Kα and a PHOTON III M14 detector.

DSC (TA, DSC 25) experiments were conducted at a heating rate of 10 K min^{-1} in a temperature range of 200–600 K in nitrogen atmosphere. TGA and DTA experiments were performed on a thermogravimetric analyzer (TA Instrument) in the temperature range of 300–870 K with the same heating rate. The type of fan used in experiment was Al.

The NMR spectra of $[NH_3(CH_2)_3NH_3]CdBr_4$ crystals were measured on a 400 MHz Avance II+ Bruker solid-state NMR spectrometer at the Western Seoul Center of KBSI. The MAS ^1H and ^{13}C NMR experiments were conducted at the Larmor frequencies of 400.13 and 100.61 MHz, respectively. To minimize the spinning sideband, a MAS rate of 10 kHz was employed. Tetramethylsilane (TMS) was used as the standard to record the NMR spectra. $T_{1\rho}$ values were measured using the $\pi/2 - \tau$ sequence method by varying spin-locking pulses. The width of the $\pi/2$ pulse for ^1H and ^{13}C was 3.56–3.72 μs. Further, static ^{14}N NMR and ^{113}Cd NMR spectra of a $[NH_3(CH_2)_3NH_3]CdBr_4$ single crystal were measured at Larmor frequencies of 28.90 and 88.75 MHz, respectively, and the chemical shift was referenced with respect to NH_3NO_3 and $CdCl_2O_8 \cdot 6H_2O$ as standard samples, respectively. The ^{14}N NMR experiments were performed using a solid-state echo sequence. An almost constant temperature within error range ±0.5 K was maintained, even when the rate of flow of nitrogen gas and the heater current were adjusted.

The ferroelastic domain pattern in the (001) plane was studied using an optical polarizing microscope. A hot stage (Linkam, THMS 600) and temperature controller maintained the temperature of the crystal.

III. Results and discussion

The X-ray powder diffraction pattern of the $[NH_3(CH_2)_3NH_3]CdBr_4$ at 298 K are displayed in Fig. 1. And, the lattice constants for $[NH_3(CH_2)_3NH_3]CdBr_4$ crystal are determined to be $a = 7.711$

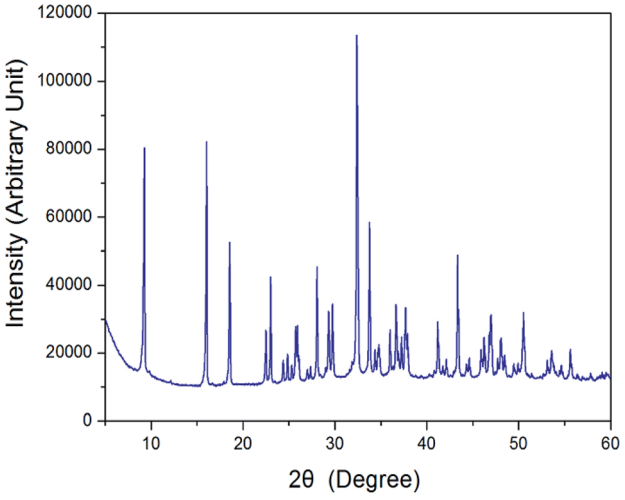

Fig. 1 X-ray diffraction pattern of the $[NH_3(CH_2)_3NH_3]CdBr_4$ crystal at 298 K.

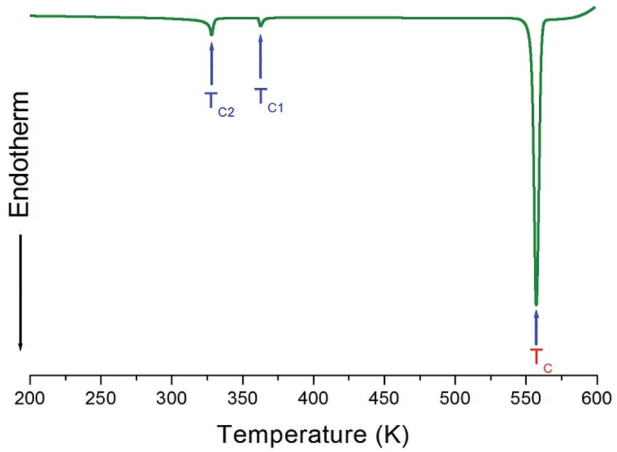

Fig. 2 Differential scanning calorimetry (DSC) thermogram of $[NH_3(CH_2)_3NH_3]CdBr_4$.

$\pm$ 0.003 Å, $b = 19.148 \pm 0.008$ Å, and $c = 7.856 \pm 0.004$ Å. This result is consistent with that reported previously.[30]

Three endothermic peaks at 328 K, 363 K, and 557 K were observed in the DSC curves of $[NH_3(CH_2)_3NH_3]CdBr_4$, as shown in Fig. 2. Two endothermic peaks at 328 K and 363 K are consistent with those previously reported by Staskiewicz *et al.*[30] In order to understand the peak of 557 K, we performed the TGA and DTA experiments and the results are presented in Fig. 3. On the DTA curve, two small endothermic peaks at 328 and 363 K are assigned to the structural phase transitions detected in the DSC experiment. A large endothermic peak at 557 K is assigned to the onset of thermal decomposition temperature ($=T_d$) by the DTA and a polarizing microscope experiments. This was characterized by a loss in the weight of the compound. It was observed that $[NH_3(CH_2)_3NH_3]CdBr_4$ ($M^w = 508.16$ mg) crystals begin to lose weight as the temperature rises. The amount remaining as solid residue is calculated from the molecular weights and balanced chemical reactions. $[NH_3(CH_2)_3NH_3]$

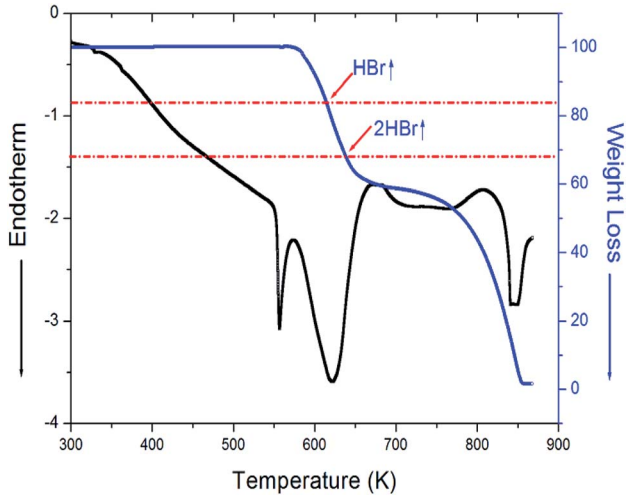

Fig. 3 Thermogravimetric analysis (TGA) and differential thermal analysis (DTA) curves for $[NH_3(CH_2)_3NH_3]CdBr_4$ crystal.

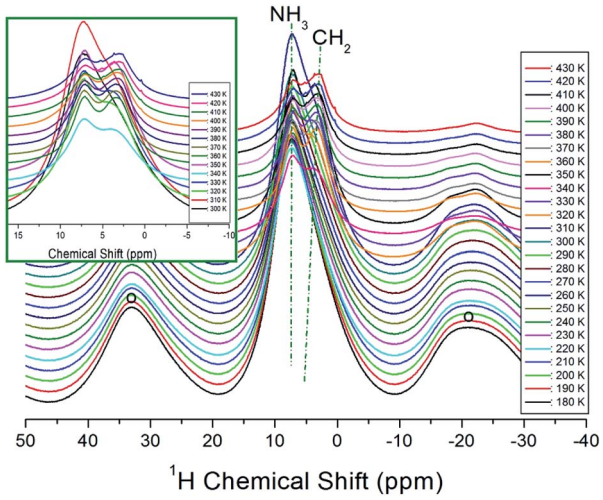

Fig. 4 *In situ* ^{1}H MAS NMR spectra for CH_2 and NH_3 of $[NH_3(CH_2)_3NH_3]CdBr_4$ at several temperatures. The spinning sidebands are marked with open circles (inset: expansion of ^{1}H NMR signals above 300 K).

$CdBr_4$ lost 16 and 32% of its weight at temperatures of approximately 614 and 638 K, respectively. The weight loss can be attributed to the decomposition of HBr and 2HBr moieties, respectively, as shown in Fig. 3. At approximately 850 K, the 98% of the total weight of this crystal is lost.

The temperature-dependent ^{1}H NMR chemical shifts for $[NH_3(CH_2)_3NH_3]CdBr_4$ crystals were recorded by MAS NMR, as shown in Fig. 4. Only one resonance signal was observed at low temperature. The observed resonance signal exhibits asymmetric shapes due to overlapping lines of the ^{1}H for two types of NH_3 and CH_2 in $[NH_3(CH_2)_3NH_3]$ cations. The spinning sidebands were marked with open circles. At 180 K, a single resonance line is present at 7.35 ppm, which subsequently splits into two resonance lines above 300 K (inset Fig. 4).

At 330 K, which is higher than T_{C2}, the NMR spectrum is separated by two resonance lines showing chemical shifts of 7.24 and 3.88 ppm for NH_3 and CH_2, respectively. The ^{1}H chemical shifts of NH_3 indicated by dotted lines in Fig. 4 are almost independent of the temperature, while those of CH_2 slightly shift toward the lower side as the temperature increases. From these results, the surrounding environment of H of NH_3 does not change depending on the temperature, and that of H of CH_2 changes slightly according to the temperature.

The ^{1}H MAS NMR spectrum was measured with respect to several delay times at each temperature. The relationship between the intensities of the NMR signals and the delay times is as follows:[33–35]

$$I(t) = I(0)\exp(-t/T_{1\rho}), \quad (1)$$

where $I(t)$ and $I(0)$ are the signal intensities at times t and $t = 0$, respectively, and $T_{1\rho}$ denotes the spin–lattice relaxation time in the rotating frame. ^{1}H NMR signals for $[NH_3(CH_2)_3NH_3]CdBr_4$ at 300 K were recorded by varying the delay times of 0.2–160 ms, as shown in the inset of Fig. 5. The decay curves were fit to

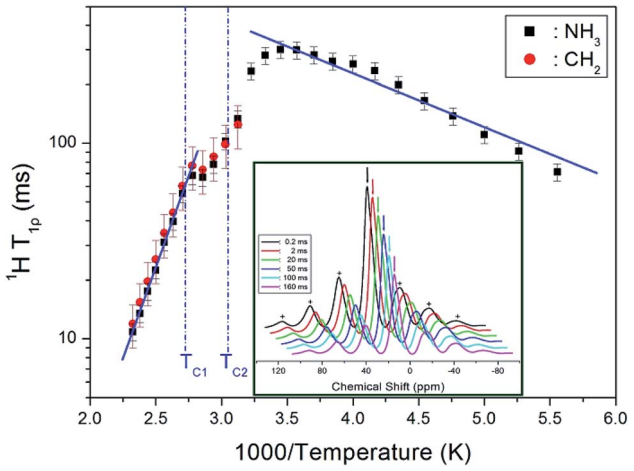

Fig. 5 ^{1}H NMR spin–lattice relaxation times $T_{1\rho}$ of $[NH_3(CH_2)_3NH_3]CdBr_4$ as a function of inverse temperature (inset: recovery curves for delay times of ^{1}H MAS NMR spectrum in $[NH_3(CH_2)_3NH_3]CdBr_4$ at 300 K).

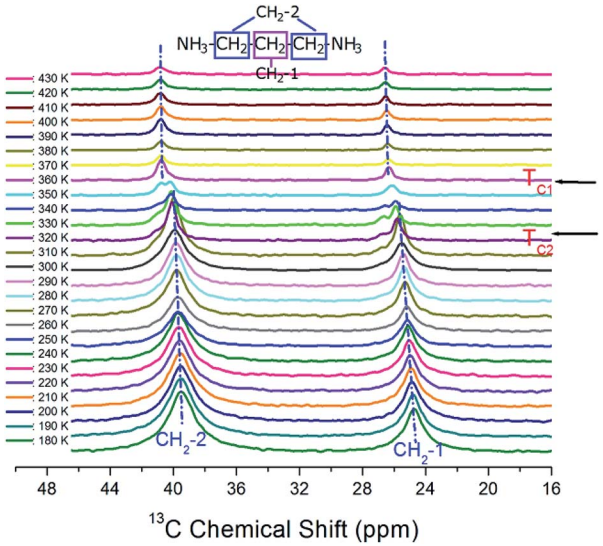

Fig. 6 *In situ* ^{13}C MAS NMR spectra for CH_2-1 and CH_2-2 of $[NH_3(CH_2)_3NH_3]CdBr_4$ as a function of temperature.

a single exponential function shown in eqn (1). The $T_{1\rho}$ values of the protons in $[NH_3(CH_2)_3NH_3]CdBr_4$ were obtained as a function of the inverse temperature, and their results are represented in Fig. 5. The $T_{1\rho}$ values initially increased and then abruptly decreased when the temperature was increased. At 328 K ($=T_{C2}$), the change in $T_{1\rho}$ values is more or less continuous; however, at approximately 363 K ($=T_{C1}$), there is a slight inflection point, marking a discontinuity. This experimental result is considered to be consistent with previously reported X-ray results,[30] stating that the *c*-value of the lattice constant is slightly shorter in the vicinity of T_{C2}, but the *c* value is rapidly shortened in the vicinity of T_{C1}. The $T_{1\rho}$ values of the protons in the $[NH_3(CH_2)_3NH_3]$ cation are 10–300 ms over the measured temperature range. At 180 K, $T_{1\rho}$ is approximately 72 ms, and at 290 K, it has a very long duration of 303 ms, and at 430 K, it exhibits a very short duration of 11 ms. The ^{1}H $T_{1\rho}$ values for NH_3 and CH_2 separated from temperatures above 320 K have highly similar values. The $T_{1\rho}$ values experience fast motion below T_{C2} and slow motion above T_{C2}. The general behavior of the $T_{1\rho}$ for random motions of the Arrhenius type with a correlation time τ_C is described in three regimes, including both fast and slow motion regimes. The fast motion regime is described as $\omega_1\tau_C \ll 1$, $T_{1\rho}^{-1} \propto \exp(E_a/k_BT)$, and the slow motion regime as $\omega_1\tau_C \gg 1$, $T_{1\rho} \propto \omega_1^{-2} \exp(-E_a/k_BT)$, where ω_1 denotes the radiofrequency power of the spin lock pulse, and E_a represents the activation energy. Different limits are satisfied for $\omega_1\tau_C$ in each of the three temperature ranges, separated by $T_{C1} =$ 363 K and $T_{C2} =$ 328 K. Specifically, the limit $\omega_1\tau_C \gg 1$ applies for both $T > T_{C1}$ and $T_{C2} < T < T_{C1}$, and the limit $\omega_1\tau_C \ll 1$ for $T < T_{C2}$. As indicated by the solid lines in Fig. 5, $E_a = 5.21 \pm 0.38$ kJ mol^{-1} at temperature below T_{C2}, while above T_{C1}, $E_a = 35.98 \pm 0.68$ kJ mol^{-1}. The decrease in $T_{1\rho}$ values with temperature indicates an increase in proton mobility at higher temperatures.

The ^{13}C MAS NMR chemical shifts in $[NH_3(CH_2)_3NH_3]CdBr_4$ were measured with respect to the change in temperature, as shown in Fig. 6. The ^{13}C MAS NMR spectrum for TMS was obtained at 38.3 ppm at 300 K. This peak at 38.3 ppm was taken as the standard and calibrated as a peak at zero ppm. Here, the CH_2 sandwiched between two other CH_2 is labeled as CH_2-1, and the CH_2 close to NH_3 is labeled CH_2-2. At 300 K, the carbon signals corresponding to the CH_2-1 and CH_2-2 in $[NH_3(CH_2)_3NH_3]CdBr_4$ appear at 25.55 and 39.96 ppm, respectively. Below T_{C2}, ^{13}C resonance signals show two resonance lines for CH_2-1 and CH_2-2. Between T_{C2} and T_{C1}, ^{13}C resonance signal was separated into three or four resonance lines. Their resonance lines at temperatures above T_{C1} were again reduced to two. Here, below T_{C2}, the chemical shifts of CH_2-1 and CH_2-2 are shifted slightly upward as the temperature increases, but at temperatures above T_{C1}, the chemical shifts of the two resonance lines are almost independent of the temperature.

The change in the full width at half maximum (FWHM) for ^{13}C NMR spectra with respect to the temperature is shown in

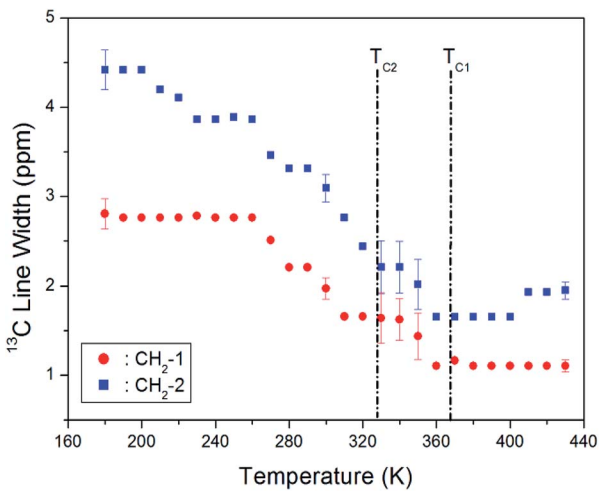

Fig. 7 Line widths of ^{13}C MAS NMR signal for CH_2-1 and CH_2-2 in $[NH_3(CH_2)_3NH_3]CdBr_4$ as a function of temperature.

Fig. 7. The ^{13}C NMR line widths for CH_2-1 and CH_2-2 decreased with an increase in temperature. The line width of the resonance line is approximately 2.8 and 4.5 ppm, respectively, for CH_2-1 and CH_2-2 at low temperature. However, as the temperature increases, the line width changes from a Gaussian to a Lorentzian shape, and it decreases rapidly. In particular, it is markedly reduced near T_{C2} and T_{C1}. The line width decreases with increasing temperature due to internal molecular motion, and that of CH_2-2 is broader than that of CH_2-1.

The intensities of ^{13}C MAS NMR signals for CH_2-1 and CH_2-2 in $[NH_3(CH_2)_3NH_3]CdBr_4$ were measured by varying the delay times at each temperature. The decay curves for CH_2-1 and CH_2-2 were fitted to a single exponential equation in eqn (1). ^{13}C $T_{1\rho}$ values were measured by the spin-locking pulse sequence with a locking pulse of 69.44 kHz. From the slope of their recovery traces, the ^{13}C $T_{1\rho}$ values were obtained for CH_2-1 and CH_2-2 as a function of 1000/temperature, as shown in Fig. 8. The values of $T_{1\rho}$ are somewhat continuous near T_{C2}, and discontinuous near T_{C1}. Similar to the results of ^1H $T_{1\rho}$, the discontinuous change near T_{C1} is consistent with the result of a rapid shortening of the lattice constant c-value. The $T_{1\rho}$ *vs.* inverse temperature curves shows minima at 32.65 and 29.14 ms for CH_2-1 and CH_2-2 at 230 K, respectively. This trend indicates that distinct molecular motions exist, where the minimum $T_{1\rho}$ was attributed to the uniaxial rotation of CH_2 ions. The $T_{1\rho}$ values were described by the correlation time τ_C for molecular motion. The $T_{1\rho}$ value for the molecular motion is given by:[34]

$$1/T_{1\rho} = C(\gamma_C{}^2\gamma_H{}^2\hbar^2/r^6)\{4\tau_C/[1+\omega_1{}^2\tau_C{}^2] + t_C/[1+(\omega_H-\omega_C)^2\tau_C{}^2] + 3\tau_C/[1+\omega_H{}^2\tau_C{}^2] + 6\tau_C/[1+(\omega_H+\omega_C)^2\tau_C{}^2] + 6\tau_C/[1+\omega_H{}^2\tau_C{}^2]\} \quad (2)$$

where C is a coefficient, γ_C and γ_H are the gyromagnetic ratios for ^{13}C and ^1H, respectively, $\hbar$ is the Planck constant, r is the distance between the proton and the carbon, ω_H and ω_C are the Larmor frequencies of ^1H and ^{13}C, respectively, and ω_1 is the spin-lock field. When $\omega_1\tau_C = 1$, $T_{1\rho}$ has a minimum value, and the coefficient of eqn (2) is obtained from the relationship between $T_{1\rho}$ and ω_1. From this coefficient, the τ_C values can be obtained relative to the temperature. The local field fluctuation is governed by the thermal motion of CH_2-1 and CH_2-2, which is activated by thermal energy. The τ_C is described by Arrhenius behavior: $\tau_C = \tau_o \exp(-E_a/k_BT)$, where τ_o, E_a, and k_B denote the pre-correlation time, activation energy of the motions, and Boltzmann constant, respectively.[33] As the magnitude of E_a depends on the molecular dynamics, we plotted on a logarithmic scale τ_C *vs.* 1000/temperature (inset of Fig. 8). Below T_{C2}, E_a values for CH_2-1 and CH_2-2 are 13.66 ± 0.58 and 14.59 ± 0.72 kJ mol^{-1}, respectively, and above T_{C1}, E_a values for CH_2-1

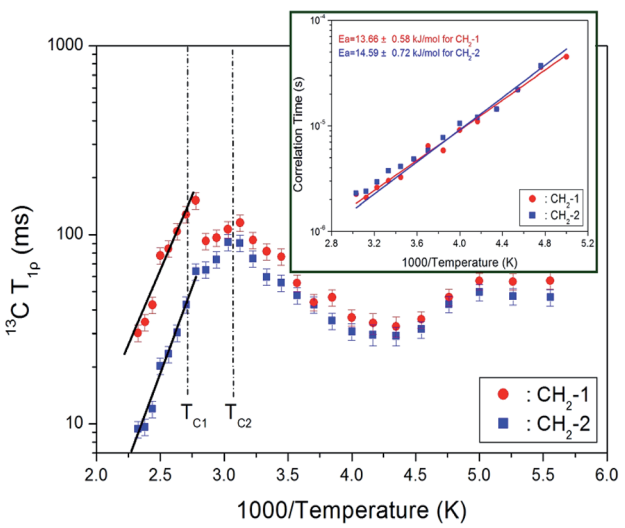

Fig. 8 ^{13}C NMR spin–lattice relaxation times $T_{1\rho}$ for CH_2-1 and CH_2-2 of $[NH_3(CH_2)_3NH_3]CdBr_4$ as a function of inverse temperature (inset: the correlation times for CH_2-1 and CH_2-2 as a function of inverse temperature).

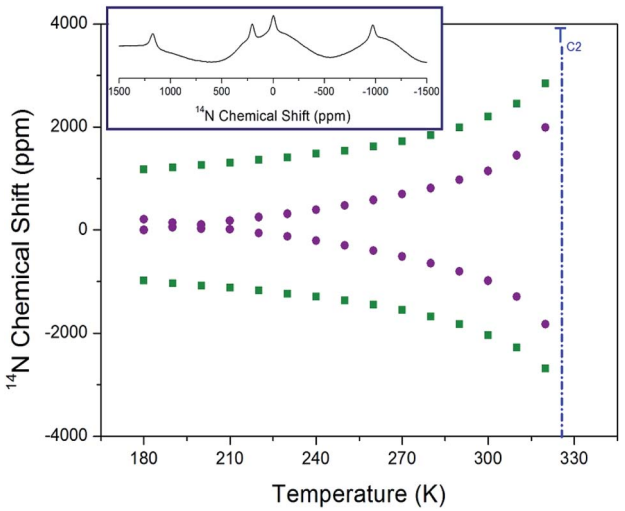

Fig. 9 Static ^{14}N chemical shifts of $[NH_3(CH_2)_3NH_3]CdBr_4$ single crystal as a function of temperature (inset: ^{14}N chemical shift at 180 K).

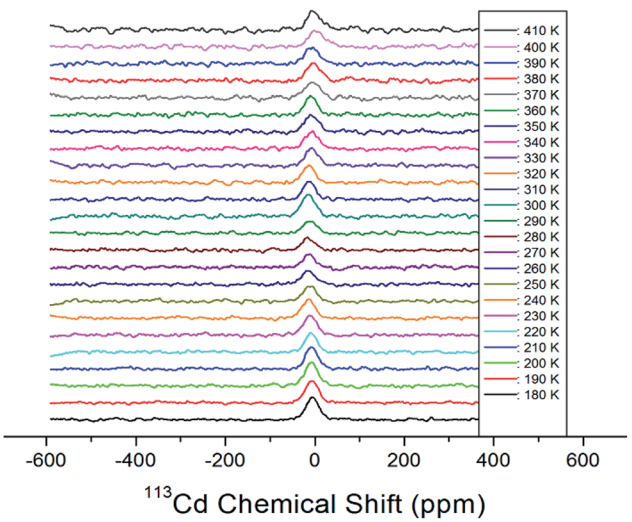

Fig. 10 Static ^{113}Cd chemical shifts of $[NH_3(CH_2)_3NH_3]CdBr_4$ single crystal as a function of temperature.

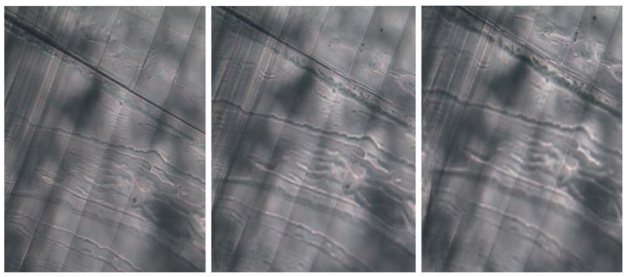

Fig. 11 Ferroelastic domain wall patterns of $[NH_3(CH_2)_3NH_3]CdBr_4$ crystal at (a) phase III (297 K), (b) phase II (333 K), and (c) phase I (383 K).

and CH_2-2 are 30.34 ± 3.41 and 35.64 ± 2.16 kJ mol^{-1}, respectively.

Static ^{14}N NMR investigations of $[NH_3(CH_2)_3NH_3]CdBr_4$ single crystal were conducted over the temperature range of 180–430 K. The ^{14}N spectra obtained using the solid-state echo method by static NMR is shown in Fig. 9. Two ^{14}N NMR signals were recorded from the quadrupole interactions due to the spin number $I = 1$. The lines with the same color below T_{C2} indicate the same pairs for ^{14}N. Near 328 K ($=T_{C2}$), the number of resonance lines and chemical shifts of the NMR spectrum showed abrupt changes. The changes in the ^{14}N chemical shift as a function of temperature were attributed to variations in the structural geometry. The chemical shift of the ^{14}N signals below T_{C2} exhibited almost continuous change, and it was difficult to observe the N signal due to the wider line width above the T_{C2} temperature. Near T_{C2}, the electric field gradient tensors at N sites varied, reflecting changes in the atomic configuration around the nitrogen atom. The environment around ^{14}N in the NH_3 groups indicates that the change is large near T_{C2}. Furthermore, at the temperature below T_{C2}, two different ^{14}N spectra were explained as follows. According to previously reported X-ray results,[30] there are no reports related to two different N sites, whereas there are reports of twin domain observations; therefore, the two different N sites are attributed to the twin domain.

Static ^{113}Cd NMR experiments were employed to examine the structural environment in $CdBr_6$ anions of the $[NH_3(CH_2)_3NH_3]CdBr_4$ single crystal. The spectrum exhibits only one peak due to the spin of $I = 1/2$. ^{113}Cd NMR spectra were obtained at several temperatures, as shown in Fig. 10. The NMR chemical shift was recorded using $CdCl_2O_8 \cdot 6H_2O$ as the standard. At 300 K, the line width is 37.95 ppm. As shown in Fig. 10, the chemical shifts for ^{113}Cd are almost constant for temperatures increasing from 180 to 410 K. This result indicates that the environment of the Cd atom surrounded by six Br atoms does not change with increasing temperature.

A crystal is ferroelastic when it has two or more orientation states in the absence of mechanical stress, and is capable to shift from one to another by mechanical stress. Several parallel lines representing ferroelastic twin domain walls are present at room temperature phase III (Fig. 11(a)), and we did not observe any changes to the domain pattern in phase II. The symmetry of phase II remains orthorhombic, and the domain wall is preserved (Fig. 11(b)). Similarly, the same domain pattern was observed in the monoclinic phase I (Fig. 11(c)). The twin boundary exists in the same direction at all temperatures. Here, the $[NH_3(CH_2)_3NH_3]CdBr_4$ crystal exists in two crystallographic phases: monoclinic (2/*m*) above 363 K, orthorhombic (*mmm*) between 328 and 363 K, and orthorhombic (*mmm*) below 328 K. For the transition from the *mmm* of the orthorhombic phase to the 2/*m* of the monoclinic phase, the domain wall orientations were expressed as $x = 0$ and $z = 0$. According to Aizu[36] and Sapriel,[37] the equations of the twin domain walls are reflected the ferroelasticity of *mmmF*2/*m*. In this case, this corresponds to "inverse" *mmmF*2/*m* suggested by Prezeslawski *et al.*,[14] unlike the *mmmF*2/*m* reported by Sapriel. Hence, our results support

Table 1 Structure, space group, lattice constant (Å), phase transition temperature T_C (K), thermal decomposition temperature T_d (K), ^1H spin–lattice relaxation time $T_{1\rho}$ (ms), ^{13}C spin–lattice relaxation time $T_{1\rho}$ (ms), and activation energies E_a (kJ mol^{-1}) for ^1H and ^{13}C in $[NH_3(CH_2)_3NH_3]CdBr_4$ and $[NH_3(CH_2)_3NH_3]CdCl_4$ crystals

	$[NH_3(CH_2)_3NH_3]CdBr_4$	$[NH_3(CH_2)_3NH_3]CdCl_4$
Structure	Orthorhombic	Orthorhombic
Space group	*Pnma*	*Pnma*
Lattice constant	$a = 7.711$	$a = 7.34163$
	$b = 19.148$	$b = 19.0300$
	$c = 7.856$	$c = 7.49273$
T_C	328, 363, 557	375
T_d	580	520
^1H $T1\rho$	280.16 (NH_3 and CH_3 at 300 K)	411.53 (NH_3 at 300 K)
		551.12 (CH_2 at 300 K)
^{13}C $T1\rho$	81.59 (CH_2-1 at 300 K)	37.13 (CH_2-1 at 300 K)
	59.80 (CH_2-2 at 300 K)	29.13 (CH_2-2 at 300 K)
^1H E_a	35.98 (phase I)	25.36 (phase I)
	5.21 (phase III)	8.37 (phase II)
^{13}C E_a (CH_2-1)	30.34 (phase I)	10.18 (phase I)
	13.66 (phase III)	29.96 (phase II)
^{13}C E_a (CH_2-2)	35.64 (phase I)	8.45 (phase I)
	14.59 (phase III)	39.94 (phase II)

the mechanism of ferroelastic twin domains. Further, the two types of inequivalent ^{14}N NMR lines are attributed to the ferroelastic twin domain structure.

IV. Conclusions

We considered the physical properties of organic–inorganic hybrid perovskite $[(NH_3)(CH_2)_3(NH_3)]CdBr_4$ crystals. First, the structure and phase transition temperatures (328 K and 363 K) were confirmed by X-ray diffraction and DSC experiments, respectively. We found that the TGA curve exhibits stability until 557 K. Second, the ^1H NMR chemical shifts of CH_2 for crystallographic environments changed more significantly with temperature than those for NH_3. At temperatures below T_{C2}, the ^{13}C chemical shifts change to a slightly upward chemical shift, whereas above T_{C1}, the chemical shift hardly changes. Furthermore, the ^{14}N chemical shift changes with temperature, whereas the ^{113}Cd chemical shift is independent of it. This is because the environments around N change, while the ^{113}Cd chemical shifts were not attributed to the rotation of $CdBr_6$ octahedra. Finally, ^1H $T_{1\rho}$ shows fast motion at low temperature and slow motion at high temperature, while ^{13}C $T_{1\rho}$ shows molecular motion at low temperature and slow motion at high temperature. Shorter $T_{1\rho}$ values at high temperature indicate that ^1H and ^{13}C in the organic chains are more flexible at these temperatures.

We compared the physical properties of the previously reported $[(NH_3)(CH_2)_3(NH_3)]CdCl_4$ crystals,[38] and those of $[NH_3(CH_2)_3NH_3]CdBr_4$ examined in this study. This is summarized in Table 1. The decomposition temperature of $[NH_3(CH_2)_3NH_3]CdBr_4$ is higher than that of $[NH_3(CH_2)_3NH_3]CdCl_4$. In the two compounds, the tendency of the ^1H and ^{13}C $T_{1\rho}$ values in terms of the temperature change is very similar, while their activation energies are very different, as shown in Table 1; $[NH_3(CH_2)_3NH_3]CdBr_4$ has a large E_a at high temperatures, whereas $[NH_3(CH_2)_3NH_3]CdCl_4$ has a large E_a at low temperature. Notably, their ^{113}Cd chemical shifts depend on the temperature change, which indicates the difference between the surrounding environments of $CdBr_6$ and $CdCl_6$ octahedra in the two compounds. Although the two crystals contain the same cations, the observed differences in structural dynamics obtained from the chemical shifts and $T_{1\rho}$ values of the two compounds can be attributed to the differences in halogen atoms Br^- and Cl^- surrounding of Cd. These results provide insights into the molecular dynamics of the $[NH_3(CH_2)_3NH_3]CdBr_4$ crystals, and are expected to facilitate their potential applications.

Conflicts of interest

There are no conflicts to declare.

Acknowledgements

This research was supported by the Basic Science Research program through the National Research Foundation of Korea, funded by the Ministry of Education, Science, and Technology (grant numbers 2018R1D1A1B07041593 and 2016R1A6A1A03012069).

References

1 R. Kind, S. Plesko, P. Gunter, J. Ross and J. Fousek, *Phys. Rev. B: Condens. Matter Mater. Phys.*, 1981, **23**, 5301.
2 D. B. Mitzi, K. Chondroudis and C. R. Kagan, *IBM J. Res. Dev.*, 2001, **45**, 29.
3 D. B. Mitzi, *J. Chem. Soc., Dalton Trans.*, 2001, **1**, 1.
4 K. Pradeesh, J. J. Baumberg and G. Vijaya Prakash, *Appl. Phys. Lett.*, 2009, **95**, 173305.
5 Z. Cheng and J. Lin, *CrystEngComm*, 2010, **12**, 2646.
6 K. Pradeesh, G. S. Yadav, M. Singh and G. Vijaya Prakash, *Mater. Chem. Phys.*, 2010, **124**, 44.
7 H.-Y. Zhang, X.-J. Song, H. Cheng, Y.-L. Zeng, Y. Zhang, P.-F. li, W.-Q. Liao and R.-G. Xiong, *J. Am. Chem. Soc.*, 2020, **142**, 4604.
8 X. Zhang, J.-X. Shen, M. E. Turiansky and C. G. Van de Walle, *Nat. Mater.*, 2021, **60**, 8198.
9 S. Saikumar, J. J. Ahmad, G. Baumberg and G. Vijaya Prakash, *Scr. Mater.*, 2012, **67**, 834.
10 B. Staskiewicz, O. Czupinski and Z. Czapla, *J. Mol. Struct.*, 2014, **1074**, 723.
11 B. Staskieqicz, I. Turowska-Tyrk, J. Baran, Cz. Gorecki and Z. Czapla, *J. Phys. Chem. Solids*, 2014, **75**, 1305.
12 S. Ahmad, C. Hanmandlu, P. K. Kanaujia and G. Vijaya Prakash, *Opt. Mater. Express*, 2014, **4**, 1313.
13 S. Gonzalez-Carrero, R. E. Galian and J. Perez-Prieto, *Part. Part. Syst. Charact.*, 2015, **32**, 709.
14 J. Prezeslawski, Z. Czapla, M. Crofton and S. Dacko, *Ferroelectrics*, 2018, **534**, 220.
15 H. Arend, K. Tichy, K. Baberschke and F. Rys, *Solid State Commun.*, 1976, **18**, 999.
16 S. Skaarup and R. W. J. Berg, *Solid State Chem.*, 1978, **26**, 59.
17 C. Sourisseau and G. Lucazeau, *J. Raman Spectrosc.*, 1979, **8**, 311.
18 H. von Kanel, *Phys. B*, 1979, **96**, 167.
19 C. Sourisseau, G. Lucazeau and A. J. Dianoux, *J. Phys.*, 1983, **44**, 967.
20 K. Chhor, J. F. Bocquet and C. Pommier, *J. Chem. Thermodyn.*, 1985, **17**, 379.
21 V. V. Eremenko, V. I. Fomin and V. S. Kurnosov, *Phys. B*, 1994, **194–196**, 187.
22 J.-C. Bissey, N. Filloleau, N.-B. Chanh, R. Berger and S. Flandrois, *Solid State Commun.*, 1998, **106**, 385.
23 M. M. Bogdan, M. I. Kobets and E. N. Khats'ko, *Low Temp. Phys.*, 1999, **25**, 192.
24 I. M. Hermes, S. A. Bretschneider, V. W. Bergmann, D. Li, A. J. Klasen, W. Mars, F. Tremel, H.-J. Laquai, M. M. Butt, R. Berger, B. J. Rodriguez and S. A. L. Weber, *J. Phys. Chem. C*, 2016, **120**, 5724.
25 E. Strelcov, Q. Dong, T. Li, J. Chae, Y. Shao, Y. Deng, A. Gruverman, J. Huang and A. Centrone, *Sci. Adv.*, 2017, **3**, e1602165.
26 Y. Liu, L. Collins, R. Proksch, S. Kim, B. R. Watson, B. Doughty, T. R. Calhoun, M. Ahmadi, A. V. Levlev, S. Jesse, S. T. Retterer, A. Belianinov, K. Xiao, J. Huang, B. G. Sumpter, S. V. Kalinin, B. Hu and O. S. Ovchinnikova, *Nat. Mater.*, 2018, **17**, 1013.

27 D.-W. Fu, J.-X. Gao, P.-Z. Huang, R.-Y. Ren, T. Shao, L.-J. Han, J. Liu and J.-M. Gong, *Angew. Chem.*, 2020, **59**, 17477.
28 M. Elseman, A. E. Shalan, S. Sajid, M. M. Rashad, A. M. Hassan and M. Li, *ACS Appl. Mater. Interfaces*, 2018, **10**, 11699–11707.
29 J. A. Aramburu, P. Garcia-Fernandez, N. R. Mathiesen, J. M. Garcia –Lastra and M. Moreno, *J. Phys. Chem. C*, 2018, **122**, 5071–5082.
30 B. Staskiewicz and A. Staskiewicz, *J. Phys. Chem. Solids*, 2017, **106**, 65.
31 H. Ishihara, S.-Q. Dou, K. Horiuchi, V. G. Krishnan, H. Paulus, H. Fuess and Al. Weiss, *Z. Naturforsch., A: Phys. Sci.*, 1996, **51**, 1216.
32 H. Ishihara, K. Horiuchi, K. Yamada, T. Okuda, V. G. Krishnan and Al. Weiss, *Chem. Lett.*, 1996, 371.
33 A. Abragam, *The Principles of Nuclear Magnetism*, Oxford University Press, 1961.
34 J. L. Koenig, *Spectroscopy of Polymers*, Elsevier, New York, 1999.
35 R. K. Harris, *Nuclear Magnetic Resonance Spectroscopy*, Pitman Pub., UK, 1983.
36 K. Aizu, *Phys. Rev. B: Solid State*, 1970, **2**, 754.
37 J. Sapriel, *Phys. Rev. B: Solid State*, 1975, **12**, 5128.
38 A. R. Lim, *J. Solid State Chem.*, 2021, **295**, 121909.